Journal of Luminescence 214 (2019) 116589

Contents lists available at ScienceDirect

Journal of Luminescence

journal homepage: www.elsevier.com/locate/jlumin

Two-dimensional axisymmetric opto-thermal phosphor modeling based on fluorescent radiative transfer equation

Yupu Ma, Xiaobing Luo*

School of Energy and Power Engineering, Huazhong University of Science and Technology Wuhan, 430074, China

ARTICLE INFO

Keywords:
Phosphor modeling
Radiative transfer
Fluorescence
Phosphor thermal quenching
Scattering

ABSTRACT

Remote phosphor plate excited by the light-emitting diode (LED) or laser diode (LD) has been widely applied in solid-state lighting. The light propagation properties within the phosphor have been analytically characterized based on the one-dimensional assumption. However, this may be not feasible in some cases, e.g., the excitation spot diameter is comparable to the plate thickness or the incident irradiance is not uniform along the horizontal direction. In this work, we extend the one-dimensional model to a two-dimensional axisymmetric opto-thermal model based on the fluorescent radiative transfer equations (FRTEs) for the cylindrical phosphor plate excited by a collimated beam with a small spot diameter and Gaussian irradiance distribution. The radiances of the blue and yellow lights are iteratively calculated by solving FRTEs in the cylindrical coordinate system using the discontinuous spectral element method. By inputting the obtained heat generation density from FRTEs, we calculate the three-dimensional temperature distribution by solving the heat diffusion equation (HDE). In addition, the opto-thermal interaction between FRTEs and HDE is achieved by introducing the temperature-dependent phosphor quantum efficiency. Using the model, we evaluate the optical, thermal and opto-thermal interacted performances of the phosphor. Finally, the model is validated by comparing the measured output optical power and surface temperature distribution with the calculated results.

1. Introduction

Light-emitting diodes (LEDs) have dominated the solid-state lighting (SSL) in the last decade [1,2]. However, LEDs have been known to suffer from efficiency droop under high current density [3]. As an alternative of SSL, laser diode (LD) possesses even higher efficiency at high current density [4] and have been a promising light source in high-power and high-luminance illumination. To obtain white light, a blue InGaN LED or LD is usually applied to excite a yellow cerium-doped yttrium aluminum garnet (YAG:Ce) phosphor, which is termed as the phosphor-converted LED (pc-LED) or phosphor-converted LD (pc-LD), respectively. In pc-LED and pc-LD, the remote phosphor in a cylindrical shape is a very common configuration, namely the phosphor is far away from the light source. Especially for pc-LD, this is the only accepted packaging form to prevent the thermal damage from LD with extremely high heat load density [5].

Light propagation properties in the phosphor, including the light absorption, scattering, and fluorescence, have determined the output optical performances [6]. Researchers have made great effort to develop numerical and analytical methods to present a deep understanding of these properties. In the numerical method based on Monto-Carlo ray-tracing simulation [7-9], accurate estimations of the optical performances can be obtained at the sacrifice of the computing efficiency though. In the analytical methods [10-13], the phosphor plate is usually assumed to be a one-dimensional geometry considering the large ratio of the diameter to the plate thickness. This assumption can greatly simplify the computing process and can also obtain accurate results in some simple cases. However, it may have a limitation in evaluating the three-dimensional internal distribution of the optical quantities and also the effect of the incident light properties. Especially for pc-LDs, the incident light is usually collimated to excite the remote phosphor so as to obtain high luminance [14]. In this case, the spot size may be comparable to the thickness and the irradiance distribution exhibits a Gaussian pattern rather than a uniform one [15], both making the one-dimensional assumption not applicable. For a cylindrical phosphor plate with axis-symmetry, the actual three-dimensional geometry can be reduced to a two-dimensional axisymmetric one, which can greatly save computing time and resource. Hence, it's essential to extend the one-dimensional model to a two-dimensional axisymmetric model to obtain more realistic and accurate results.

In addition to the light propagation, the thermal transport in the phosphor is also of concern. Besides the light-to-light process, there is

* Corresponding author.
E-mail address: luoxb@hust.edu.cn (X. Luo).

https://doi.org/10.1016/j.jlumin.2019.116589
Received 14 April 2019; Received in revised form 25 May 2019; Accepted 28 June 2019
Available online 29 June 2019
0022-2313/ © 2019 Elsevier B.V. All rights reserved.

also the light-to-heat process, which mainly consists of the Stokes shift loss and quantum efficiency loss [16]. The heat generation in the phosphor can be obtained using the above phosphor modeling methods. In most previous studies [17,18], the phosphor temperature distribution is obtained by inputting the heat generation as a uniform heat source into the heat diffusion equation (HDE), which is then solved by the finite-element thermal simulation. Considering the distributed light quantities inside the phosphor, the uniform heat source treatment may cause large deviation with the actual case.

To tackle this problem, some researchers have obtained the heat generation density using the commercial ray-tracing software ASAP [19] or LightTools together with a user-created phosphor particle [9]. Besides the ray-tracing method, Lenef et al. have also calculated the heat generation density and then the temperature distribution by combining the diffusion approximation (DA) method with the thermal simulation [14,15]. It should be noted that the heat generation density and the phosphor temperature may be relatively low for most pc-LEDs. However, for pc-LDs, the phosphor temperature may easily exceed the quenching temperature point under collimated incidence with high excitation optical density [20]. In this case, there exists an opto-thermal interaction between the reduced quantum efficiency and increased phosphor temperature. Hence, this interaction needs to be considered to evaluate the thermal quenching effect [9,14].

In this work, we extend our previous one-dimensional optical model [10] to a two-dimensional axisymmetric opto-thermal model based on the fluorescent radiative transfer equations (FRTEs) for a cylindrical phosphor excited by a collimated LD beam with Gaussian irradiance distribution. The model is established by simultaneously solving FRTEs of the excitation blue light and emission yellow lights and HDE in the cylindrical coordinate system. In addition, we introduce the temperature-dependent phosphor quantum efficiency to achieve the opto-thermal interaction between FRTEs and HDE. Compared with the stochastic numerical tools [9,19], the presented model is more favorable in terms of high computational efficiency. Compared with the DA method which fails to model such media with significant absorption characteristic [14,15], the presented model can be applied to the fluorescent media with high concentration and high absorption. Moreover, DA method cannot return the radiance distribution, which can be obtained using the presented method. The optical, thermal, and opto-thermal interacted performances are evaluated using the presented opto-thermal model, which is finally validated by experiments.

2. Model definition

In this section, we define the two-dimensional axisymmetric opto-thermal phosphor model in the sequence of the governing equations, boundary conditions, and the numerical implementation method.

2.1. Governing equations

The light propagation properties in the cylindrical phosphor can be described by FRTEs for the excitation blue and the emission yellow lights in the cylindrical coordinate system (shown in Fig. 1) [10,11,21]:

$$\frac{\eta}{r}\frac{\partial}{\partial r}[rI_B(\mathbf{r},\mathbf{\Omega})]+\frac{\xi}{r}\frac{\partial}{\partial \psi}[I_B(\mathbf{r},\mathbf{\Omega})]+\mu\frac{\partial}{\partial z}[I_B(\mathbf{r},\mathbf{\Omega})]-\frac{1}{r}\frac{\partial}{\partial \phi}[\xi I_B(\mathbf{r},\mathbf{\Omega})]+(\kappa_B^a+\kappa_B^s)I_B(\mathbf{r},\mathbf{\Omega})=S_B \tag{1.1}$$

$$\frac{\eta}{r}\frac{\partial}{\partial r}[rI_Y(\mathbf{r},\mathbf{\Omega})]+\frac{\xi}{r}\frac{\partial}{\partial \psi}[I_Y(\mathbf{r},\mathbf{\Omega})]+\mu\frac{\partial}{\partial z}[I_Y(\mathbf{r},\mathbf{\Omega})]-\frac{1}{r}\frac{\partial}{\partial \phi}[\xi I_Y(\mathbf{r},\mathbf{\Omega})]+(\kappa_Y^a+\kappa_Y^s)I_Y(\mathbf{r},\mathbf{\Omega})=S_Y \tag{1.2}$$

where $I(\mathbf{r},\mathbf{\Omega})$ is the radiance at spatial location $\mathbf{r}(r, \Psi, z)$ and angular direction $\mathbf{\Omega}(\theta, \phi)$, and the subscripts B and Y denote the blue and yellow lights, respectively; η, ξ, and μ are respectively direction cosines along r, Ψ, and z directions; κ^a and κ^s are the absorption and scattering coefficients. The first four terms on the left side of Eq. (1) denote the radiance gradient and the last term represents the radiance decrement due to effective absorption. S_B and S_Y on the right side are the source terms for blue and yellow lights and can be respectively expressed as:

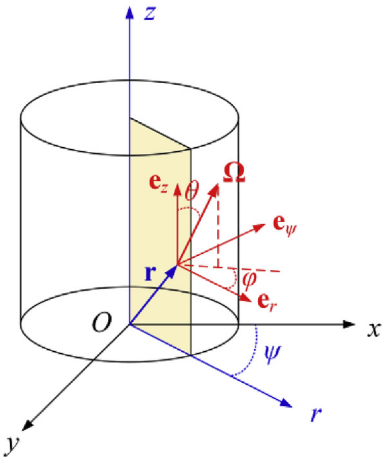

Fig. 1. The schematic of the cylindrical coordinate system.

$$S_B=\frac{\kappa_B^s}{4\pi}\int_{4\pi} I_B(\mathbf{r},\mathbf{\Omega}')p(\mathbf{\Omega},\mathbf{\Omega}')d\Omega' \tag{2.1}$$

$$S_Y=\frac{\kappa_Y^s}{4\pi}\int_{4\pi} I_Y(\mathbf{r},\mathbf{\Omega}')p(\mathbf{\Omega},\mathbf{\Omega}')d\Omega'+\frac{\eta_{con}(\mathbf{r})}{4\pi}\kappa_B^a\int_{4\pi} I_B(\mathbf{r},\mathbf{\Omega})d\Omega \tag{2.2}$$

where $p(\mathbf{\Omega},\mathbf{\Omega}')$ is the scattering phase function. S_B denotes the radiance increment due to scattering from other direction $\mathbf{\Omega}'$ to the specific direction $\mathbf{\Omega}$. S_Y not only contains this part but also the fluorescent contribution from the absorbed blue light [10], which is characterized by the phosphor conversion efficiency $\eta_{con}(\mathbf{r})=\mathrm{QE}(\mathbf{r})\cdot\lambda_B/\lambda_Y$. $\mathrm{QE}(\mathbf{r})$ and λ_B/λ_Y denote the phosphor quantum efficiency and Stokes shift efficiency, respectively, where λ_B and λ_Y are the wavelengths for the blue and yellow lights.

For an axisymmetric case, the radiance is independent of the spatial azimuth angle Ψ, namely $\partial I(\mathbf{r},\mathbf{\Omega})/\partial\Psi=0$. It should be noted that there is a singularity of $1/r$ at $r=0$ (i.e., axis). In this case, Eq. (1) is multiplied by r to avoid the numerical singularity [22]. Using the above two treatments, we can rewrite Eq. (1) as:

$$\eta\frac{\partial}{\partial r}[rI_B(\mathbf{r},\mathbf{\Omega})]+\mu\frac{\partial}{\partial z}[rI_B(\mathbf{r},\mathbf{\Omega})]-\frac{\partial}{\partial \phi}[\xi I_B(\mathbf{r},\mathbf{\Omega})]+r(\kappa_B^a+\kappa_B^s)I_B(\mathbf{r},\mathbf{\Omega})=rS_B \tag{3.1}$$

$$\eta\frac{\partial}{\partial r}[rI_Y(\mathbf{r},\mathbf{\Omega})]+\mu\frac{\partial}{\partial z}[rI_Y(\mathbf{r},\mathbf{\Omega})]-\frac{\partial}{\partial \phi}[\xi I_Y(\mathbf{r},\mathbf{\Omega})]+r(\kappa_Y^a+\kappa_Y^s)I_Y(\mathbf{r},\mathbf{\Omega})=rS_Y \tag{3.2}$$

The thermal transport property in the two-dimensional axisymmetric phosphor is governed by the steady-state heat diffusion equation:

$$\frac{1}{r}\frac{\partial}{\partial r}\left[kr\frac{\partial T(\mathbf{r})}{\partial r}\right]+\frac{\partial}{\partial z}\left[k\frac{\partial T(\mathbf{r})}{\partial z}\right]=-q(\mathbf{r}) \tag{4}$$

where $T(\mathbf{r})$ is the temperature distribution at the spatial location $\mathbf{r}$; k is the thermal conductivity and assumed to be independent of $\mathbf{r}$ in most cases [1]; $q(\mathbf{r})$ denotes the heat source and can be obtained by solving the above FRTEs, which will be illustrated in the following part.

2.2. Boundary definitions

Fig. 2 shows the schematic of the phosphor model. Considering a cylindrical phosphor plate illuminated by a circular spot, the three-dimensional model can be reduced to a two-dimensional axisymmetric

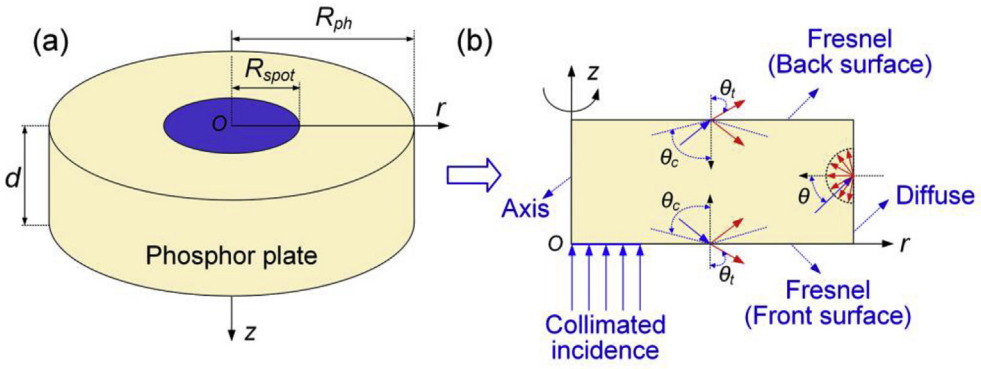

Fig. 2. The schematic of the simplification from the (a) three-dimensional phosphor model to (b) a two-dimensional axisymmetric model together with the boundary conditions, including the symmetric axis, collimated incidence on the front surface, Fresnel boundary on the front and back surfaces, and the diffuse boundary on the cylindrical surface.

model featured by the radial and axial coordinate r and z. As shown in Fig. 2, due to the axis-symmetry, the cross-section r-z surface at arbitrary spatial azimuth angle Ψ is chosen as the solution domain with dimensions of $[0, R_{ph}] \times [0, d]$, where R_{ph} and d are the radius and thickness of the phosphor plate, respectively. The basic variable to be solved is the radiance $I(r, z, \theta, \phi)$, which is dependent of two spatial variables (r and z) and two angular variables (θ and ϕ).

The boundary conditions are illustrated in Fig. 2(b). It can be easily seen that the rectangle domain contains four boundaries. The left boundary (axis) is an imaginary mathematical boundary or called pole boundary. According to the method proposed by Zhang et al. [22], the pole boundary can be obtained by setting r → 0 in Eq. (3) and yields:

$$\eta I_i(0, z, \mathbf{\Omega}) - \frac{\partial}{\partial \phi}[\xi I_i(0, z, \mathbf{\Omega})] = 0,\ i = B\ or\ Y \tag{5}$$

Other three boundaries are the same as the physical boundaries in the three-dimensional case. The front surface (facing the light source) and back surface are considered to be Fresnel surfaces. In this case, when the light travels from the dense medium ($n > 1$) to the surrounding air ($n=1$), total reflection and refraction will happen simultaneously. The details of the Fresnel boundary can be found in our previous work [10]. There is also an incidence on the front surface. In this work, we focus on the collimated incidence with Gaussian irradiance profile, which is the typical emission pattern from LD. It can be expressed as:

$$I_B(r, 0, \mathbf{\Omega}) = I_0 \exp\left(\frac{-2r^2}{w^2}\right) = \frac{2P}{\pi w^2}\exp\left(\frac{-2r^2}{w^2}\right),\ \mathbf{\Omega}\cdot\mathbf{n}_w = 1, 0 \le r \le R_{spot} \tag{6}$$

where P and w denote the total incident power and beam waist; $\mathbf{n}_w$ is the unit inward normal vector at the front surface; R_{spot} is the radius of the spot. It should be pointed out other types of incidence can also be applied, including the diffuse incidence and Lambertian incidence. When it comes to the practical case, e.g., a laser diode bar exhibiting quadrant symmetry emission pattern is used, the rotationally symmetric assumption may pose effect on the optical and thermal performances. But we think this may be within an acceptable range, especially considering the increased complexity and computational time of developing a full three-dimensional model. As for the right boundary corresponding to the outer cylindrical surface, the diffuse reflection boundary, on which the light is reflected isotropically, is applied for simplicity. This may be feasible because the phosphor plate is usually placed into a reflector or holder.

Besides the above optical boundaries, the thermal boundaries are also defined. To be consistent with the optical boundaries, the front and back surfaces are set to be Robin boundaries:

$$-k\mathbf{n}_w\cdot\nabla T(\mathbf{r}) = h(T_w - T_\infty) \tag{7}$$

where T_w is the temperature distribution on the boundary; h and T denote the convective heat transfer coefficient and the ambient temperature, respectively. The cylindrical surface is set to be a Dirichlet or Neumann boundary depending on the actual heat dissipation condition.

2.3. Numerical implementation

It can be seen that FRTEs are partial differential-integral equations and exact analytical solutions only exist in very simple cases. Here, the discontinuous spectral element method (DSEM), which has been successfully applied in solving RTE [23], is extended to solve the two-dimensional axisymmetric FRTEs together with the boundary conditions.

Different from the FRTEs in the Cartesian coordinate system, Eq. (3) contains an angular redistribution term (the third term on the left side) due to the connection of the definition of angular coordinates with spatial coordinates [22]. Following the same method presented in [22,24], finite difference discretization together with the piecewise constant angular approximation (PCA) method is applied. In this way, we obtain the discrete ordinate form of the FRTEs as:

$$\eta^{m,n}\frac{\partial(rI_B^{m,n})}{\partial r} + \mu^{m,n}\frac{\partial(rI_B^{m,n})}{\partial z} + \overline{\beta}_B^{m,n}(r)I_B^{m,n} = \overline{S}_B^{m,n} \tag{8.1}$$

$$\eta^{m,n}\frac{\partial(rI_Y^{m,n})}{\partial r} + \mu^{m,n}\frac{\partial(rI_Y^{m,n})}{\partial z} + \overline{\beta}_Y^{m,n}(r)I_Y^{m,n} = \overline{S}_Y^{m,n}(r) \tag{8.2}$$

where

$$\overline{\beta}_B^{m,n} = r\left(\kappa_B^a + \kappa_B^s - \frac{\kappa_B^s}{4\pi}p^{m,n;m,n}\omega_\theta^m\omega_\phi^m\right) + \frac{1}{\omega_\theta^n}\left[\max\left(\chi_\phi^{m,n+1/2}, 0\right) + \max\left(-\chi_\phi^{m,n-1/2}, 0\right)\right] \tag{9.1}$$

$$\overline{\beta}_Y^{m,n} = r\left(\kappa_Y^a + \kappa_Y^s - \frac{\kappa_Y^s}{4\pi}p^{m,n;m,n}\omega_\theta^m\omega_\phi^n\right) + \frac{1}{\omega_\phi^n}\left[\max\left(\chi_\phi^{m,n+1/2}, 0\right) + \max\left(-\chi_\phi^{m,n-1/2}, 0\right)\right] \tag{9.2}$$

$$\overline{S}_B^{m,n} = \frac{1}{\omega_\phi^n}\left[\max\left(-\chi_\phi^{m,n+1/2}, 0\right)I_B^{m,n+1} + \max\left(\chi_\phi^{m,n-1/2}, 0\right)I_B^{m,n-1}\right] + r\frac{\kappa_B^S}{4\pi}\sum_{m'=1,m'\neq m}^{N_\theta}\sum_{n'=1,n'\neq n}^{N_\phi} I_B^{m',n'}p^{m',n';m,n}\omega_\theta^{m'}\omega_\phi^{n'} \tag{9.3}$$

$$\overline{S}_Y^{m,n} = \frac{1}{\omega_\phi^n}\left[\max\left(-\chi_\phi^{m,n+1/2}, 0\right)I_Y^{m,n+1} + \max\left(\chi_\phi^{m,n-1/2}, 0\right)I_Y^{m,n-1}\right] + r\left[\begin{array}{l}\frac{\kappa_Y^S}{4\pi}\sum_{m',=1,m'\neq m}^{N_\theta}\sum_{n',=1,n'\neq n}^{N_\phi}\omega_\theta^{m'}\omega_\phi^{n'} \\ +\ \frac{\eta_{con}(\mathbf{r})}{4\pi}\kappa_B^a\sum_{m'=1}^{N_\theta}\sum_{n'=1}^{N_\phi} I_B^{m',n'}\omega_\theta^{m'}\omega_\phi^{n'}\end{array}\right] \tag{9.4}$$

where N_θ and N_ϕ denote the division number of the polar and azimuthal angles, ω_θ and ω_ϕ are angular weight along the polar and azimuthal

angles. The discrete ordinate form of the pole condition [Eq. (7)] can be expressed similarly as:

$$I_i^{m,n}(0, z) = \frac{\overline{S}_i^{m,n}(0, z)}{\eta^{m,n} + \overline{\beta}_i^{m,n}(0, z)},\ i = B\ or\ Y \tag{10}$$

It should be pointed out that the collimated direction cannot be directly included in the above discrete ordinate method. Wang et al. have considered the collimated incidence in RTE by regarding the total radiance as the combination of the collimated component and the diffuse component [25]. Here, we extend this method to treat the collimated incidence in FRTEs and obtain:

$$I_i I_{i,c} + I_{i,d},\ i = B\ or\ Y \tag{11}$$

Considering the incident (or excitation) light for YAG:Ce phosphor is usually blue light, the collimated component of blue light $I_{B,c}$ decreases exponentially along the axial coordinate according to Beer's law and Eq. (6) can be re-written as:

$$I_{B,c}(r, z) = \frac{2P}{\pi w^2}\exp\left(\frac{-2r^2}{w^2}\right)\exp[-(\kappa_B^a + \kappa_B^s)z] \tag{12}$$

The governing equation of the collimated component of yellow light $I_{Y,c}$ can be obtained by setting $\eta=0$, $\mu=1$, $\partial I/\partial\phi=0$ in Eq. (3.2) and yields:

$$\frac{dI_{Y,c}(r, z)}{dz} + (\kappa_Y^a + \kappa_Y^s)\cdot I_{Y,c}(r, z) = \frac{\eta_{con}(\mathbf{r})}{4\pi}\kappa_B^a\left[\int_{4\pi} I_{B,d}(\mathbf{r}, \mathbf{\Omega})d\Omega + I_{B,c}\right] \tag{13}$$

This is a very simple first-order differential equation and can be easily solved after knowing the radiance distribution of the blue light.

To obtain the diffuse component of blue light $I_{B,d}$ and yellow light $I_{Y,d}$, the scattering contribution of the collimated component should be added to the source term in Eq. (2):

$$S_B = \frac{\kappa_B^s}{4\pi}\left[\int_{4\pi} I_{B,d}(\mathbf{r}, \mathbf{\Omega}')p(\mathbf{\Omega}, \mathbf{\Omega}')d\Omega' + I_{B,c}(\mathbf{r}, \mathbf{\Omega}_c)p(\mathbf{\Omega}_c, \mathbf{\Omega})\right] \tag{14.1}$$

$$S_Y = \frac{\kappa_Y^s}{4\pi}\left[\int_{4\pi} I_{Y,d}(\mathbf{r}, \mathbf{\Omega}')p(\mathbf{\Omega}, \mathbf{\Omega}')d\Omega' + I_{Y,c}(\mathbf{r}, \mathbf{\Omega}_c)p(\mathbf{\Omega}_c, \mathbf{\Omega})\right] + \frac{\eta_{con}(\mathbf{r})\kappa_B^a}{4\pi}\left[\int_{4\pi} I_{B,d}(\mathbf{r}, \mathbf{\Omega})d\Omega + I_{B,c}(\mathbf{r}, \mathbf{\Omega}_c)\right] \tag{14.2}$$

Fig. 3 illustrates the flowchart of solving the discrete-ordinates FRTEs under collimated incidence using DSEM. First, the parameters appearing in the governing equations and boundary conditions need to be inputted. Then, the rectangle solution domain is discretized into a number of rectangle elements and the basis function ξ_j on each element is obtained using the discontinuous Galerkin scheme. Also, the angular domain is discretized using the PCA method. Next, the collimated component of the blue light $I_{B,c}$ is solved using Eq. (13). By inputting $I_{B,c}$ as a part of source term [Eq. (14.1)], the diffuse component of blue light $I_{B,d}$ is then solved. In this process, the DSEM discretization of the discrete-ordinates FRTE for the diffuse blue light in the matrix form on each element is obtained as Eq. (15) for the specific direction $\mathbf{\Omega}^{m,n}$ using the following approximation [Eq. (16)]:

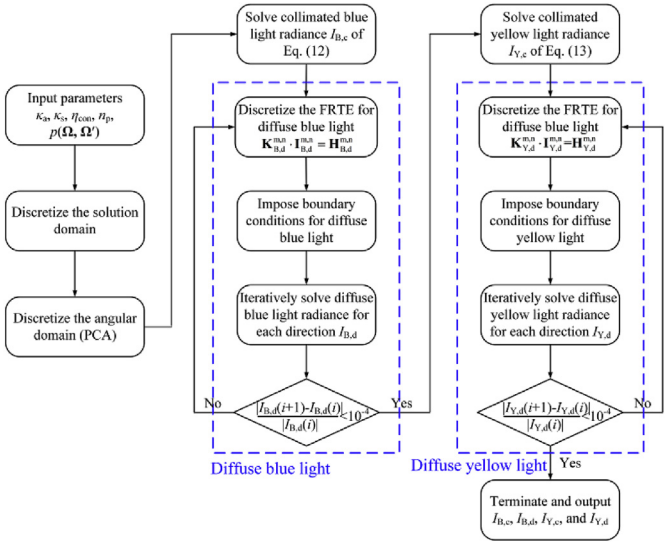

Fig. 3. The flowchart of solving the discrete-ordinates FRTEs under collimated incidence using DSEM.

$$\mathbf{K}_{i,d}^{m,n}\mathbf{I}_{i,d}^{m,n} = \mathbf{H}_{i,d}^{m,n},\ i = B\ or\ Y \tag{15}$$

$$rI_{i,d}^{m,n} = \sum_{j=1}^{N_{esol}} r_j I_{i,d,j}^{m,n}\xi_j,\ i = B\ or\ Y \tag{16}$$

where N_{esol} denotes the total number of the solution nodes of each element. More details of the matrix equation and assembling of the matrices $\mathbf{K}^{m,n}$ and $\mathbf{H}^{m,n}$ can be found in [23]. Then, impose the boundary condition of diffuse blue light. Next, begin to loop each discrete direction and solve the radiance for the diffuse blue light $I_{B,d}$ at all solution nodes along each direction simultaneously. Then, iterate over each direction until the stop criterion is satisfied. After obtaining $I_{B,c}$ and $I_{B,d}$, the collimated component of the yellow light $I_{Y,c}$ is solved using Eq. (13). Similarly, the diffuse component of the yellow light $I_{Y,d}$ is then calculated by solving the matrix equation for yellow light [Eq. (15)] using the same steps with diffuse blue light.

Finally, the calculated $I_{B,c}$, $I_{B,d}$, $I_{Y,c}$, and $I_{Y,d}$ are used to evaluate the optical performances. The radiant flux for diffuse blue light $\Phi_{B,d}$, total blue light $\Phi_{B,tot}$, diffuse yellow light $\Phi_{Y,d}$, and total yellow light $\Phi_{Y,tot}$ can be respectively expressed as:

$$\Phi_{i,d}(r, z) = \sum_{m=1}^{N_\theta}\sum_{n=1}^{N_\phi} I_{i,d}(r, z, \Omega^{m,n})\omega_\theta^m\omega_\phi^n,\ i = B\ or\ Y \tag{17.1}$$

$$\Phi_{i,tot}(r, z) = I_{i,c}(r, z) + \Phi_{i,d}(r, z),\ i = B\ or\ Y \tag{17.2}$$

According to the Fresnel boundary condition at the front and back surfaces, the output radiance with a transmitted angle θ_t at z=0 and z=d can be respectively expressed as:

$$I_{i,out}(r, 0, \theta_t, \phi) = [1 - R(\cos\theta)]I_{i,d}(r, 0, \theta, \phi),\ \cos\theta < 0,\ \theta > \theta_{c1},\ i = B\ or\ Y \tag{18.1}$$

$$I_{i,out}(r, d, \theta_t, \phi) = [1 - R(\cos\theta)]I_{i,d}(r, d, \theta, \phi),\ \cos\theta > 0,\ \theta < \theta_{c2},i = B\ or\ Y \tag{18.2}$$

where R denotes the specular reflectivity. θ_{c1} and θ_{c2} are the critical angle of the Fresnel boundary on the front and back surfaces, respectively. Then, the output optical power and correlated color temperature (CCT) can be further obtained using the output radiance [26].

In addition, the heat generation density $q(r, z)$ in the phosphor plate can be calculated as the sum of the heat generated from the absorbed radiant flux of the total blue and yellow lights [10,27,28]:

$$q(r, z) = \kappa_B^a[1 - \eta_{con}(r, z)]\Phi_{B,tot}(r, z) + \kappa_Y^a\Phi_{Y,tot}(r, z) \tag{19}$$

By inputting $q(r, z)$ into Eq. (4), we can further obtain the temperature distribution $T(r, z)$. In this work, the two-dimensional axisymmetric HDE together with the boundary condition is solved by finite element method conducted in the commercial software COMSOL. It should be noted that in the case of collimated incidence, the excitation optical energy may be very high, resulting in a high $q(r, z)$ and thus high $T(r, z)$. For phosphor, when the temperature exceeds the onset quenching temperature, the quantum efficiency starts to drop, leading to a rise of $q(r, z)$. This thermal rollover phenomenon has been known in pc-LD [20]. Here, we establish an opto-thermal coupling model by

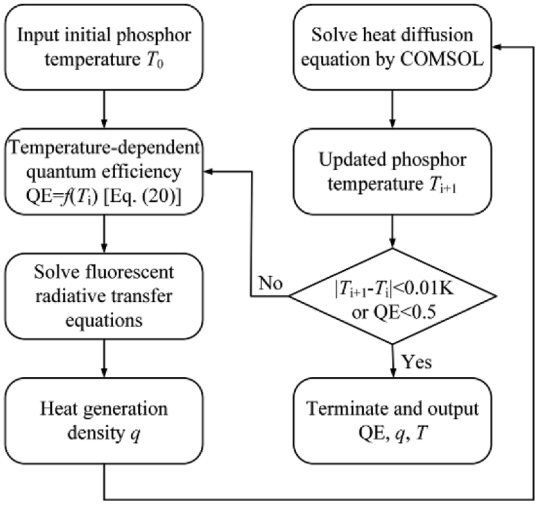

Fig. 4. The flowchart of the opto-thermal phosphor model.

introducing the temperature-dependent quantum efficiency QE(T), which can be expressed as [29,30]:

$$\mathrm{QE}(T) = \frac{\tau_{nr}(T)}{\tau_{nr}(T) + \tau_r} \tag{20}$$

where τ_r is the radiative lifetime and τ_{nr} is the non-radiative lifetime, which usually has temperature dependence. The values of τ_{nr} and τ_r for a typical YAG:Ce phosphor can be obtained in [29].

Fig. 4 shows the flowchart of the opto-thermal phosphor model. First, input the initial phosphor temperature (e.g., the ambient temperature) and then an initial QE(**r**) is obtained according to Eq. (20). By inputting QE(**r**) into the FRTEs, q can be further obtained by solving Eq. (8). Next, an updated T can be calculated by inputting the initial q into HDE. In the following, the above process is repeated until the relative temperature difference is lower than 0.01 K or the minimum quantum efficiency $\mathrm{QE}_{\min}$ is lower than 0.5. We choose the minimum value of QE as the threshold because we only focus on the illuminated area with relative lower temperature gradient. As long as $\mathrm{QE}_{\min}$ is lower than 0.5, it can be regarded that severe silicone degradation and phosphor thermal quenching occur in most of the illuminated area. The opto-thermal interaction is expected to predict the temperature distribution more accurately and further evaluate the thermal quenching effect.

3. Experiments

To verify the opto-thermal model, we fabricate a transmissive pc-LD module consisting of a commercial laser diode (L450P1600MM, Thorlabs), a collimating lens, and a cylindrical phosphor plate. As shown in Fig. 5(a), the LD is mounted into a home-made heat sink to enable a stable output power. The lens is also mounted on the heat sink. The phosphor plate (YAG:Ce phosphor embedded in silicone matrix) with a diameter of 10.0 mm and thickness of 0.5 mm is fitted into a metal mount and then supported by a holder. The height of the mount is adjusted so that the center of the phosphor plate is in line with the LD and lens. The divergent laser beam from the LD is collimated by the collimating lens and the diameter of the illuminated spot on the phosphor is measured to be about 1.0 mm. This transmissive configuration is consistent with the boundary conditions presented in Fig. 2 with Fresnel boundary on the front and back surface and diffuse boundary on the cylindrical surface.

Fig. 5(b) shows the schematic of the experimental setup of the optical test. The entire transmissive pc-LD module is positioned inside an integrating sphere (ATA-1000, Everfine), in which case both the output optical power from the front surface and back surface are collected and measured by the integrating sphere. Fig. 5(c) shows the schematic of the experimental setup of the thermal test. The temperature distribution of the back surface is captured using an infrared (IR) thermal imager (SC620, FLIR). Before the test, the surface emissivity is calibrated to be 0.94 using a thermocouple. During the test, the IR imager is positioned right in front of the back surface of the phosphor plate and adjusted to be horizontal to the target. In both optical and thermal tests, varying driving currents from 0 mA to 450 mA with an interval of 50 mA are applied. It should be pointed out that for each driving current, the output optical power and surface temperature distribution are measured for ten times under a steady-state condition. And each current experiment is done starting from room temperature. The error bar is obtained by calculating the corresponding average value and standard deviation of these data.

4. Results and discussion

To calculate the opto-thermal performances using the presented model, we need to obtain some input parameters in advance. The absorption and scattering coefficients for the blue and yellow lights with the corresponding wavelength of 445 nm and 558 nm at phosphor concentration of 0.15 g/cm^3 are respectively 1.36 mm^{-1}, 2.29 mm^{-1} and 0.01 mm^{-1}, 3.19 mm^{-1}, which are collected from our previous work [31] based on Mie theory. This set of parameters is used in all the following simulated cases. The refractive index of the phosphor plate is set to be 1.53 [1], with a corresponding critical angle of 41° in Fresnel boundary. The Henyey-Greenstein (HG) phase function with the anisotropy parameter of 0.82 is applied [10].

4.1. Optical performances

First, the optical performances are evaluated. In this section, the modeled phosphor has a radius of 2.0 mm and a thickness of 0.5 mm. The incident collimated beam has a total excitation optical power of 100 mW and a spot radius of 0.5 mm. The solution domain is divided into 8 × 2 square elements and there are 5 × 5 solution nodes in each element. In this case, there are 400 solution nodes in total. The angular domain is discretized uniformly with 64 and 32 discrete angles in the polar (θ) and azimuth (ϕ) direction, respectively. It takes about 10.1 min to finish the iterative process in Fig. 3 by MATLAB using a 3.3-GHz Intel(R) Core(TM) i3-3220 processor. Considering the total discrete numbers is as high as 8.192×10^5, the computing efficiency is still very high. The computational time increases with the number of solution nodes and discrete angles. For example, the computational time increases from 6.4 min to 10.1 min when the number of the solution nodes increases from 200 to 400. And the computing time may be reduced significantly using a more advanced processor. In addition, the computing efficiency can be further increased using the parallel computation by simultaneously solving the radiance of each element.

Fig. 6 shows the two-dimensional radiant flux distribution of different light components calculated by Eq. (17). It can be seen that the highest value of the radiant flux of the collimated blue light is located in the bottom-left corner due to the incident collimated blue light on the front surface, whereas that of the diffuse blue light is located in the middle of the left side due to the combined effect of the light scattering and Fresnel boundary on the back surface. The radiant flux of total blue light has the same distribution with that of collimated blue light because the collimated component has obviously larger values than the diffuse one. As for the yellow light, it can be seen that both the collimated and diffuse components have similar distribution with the total blue light due to the fact that the yellow light is converted from the absorbed radiant flux of the total blue light.

4.2. Opto-thermal performances

Before calculating the thermal performance, the thermal boundaries are defined as follows. The front and back surfaces have a natural

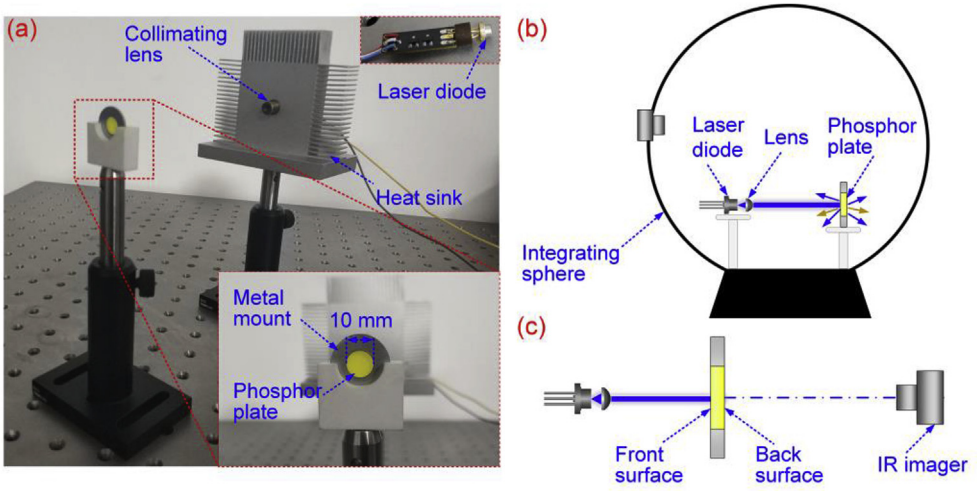

Fig. 5. (a) The photograph of the tested transmissive pc-LD module consisting a laser diode, collimating lens, and phosphor plate. The inset shows the enlarged figure of the phosphor plate fitted into a metal mount and supported by a holder. The schematic of experimental setup of the (b) optical test and (c) thermal test.

convective heat transfer coefficient of 5 W/(m^2·K). For simplicity, the cylindrical surface has a fixed temperature of 20 degC. The thermal conductivity of the phosphor plate is 0.18 W/(m·K) [27]. The following results in this section are all based on these thermal conditions.

Fig. 7 shows the three-dimensional distribution of the heat generation density q and phosphor temperature T under excitation power of 100 mW. It can be seen that q has a similar distribution with the radiant flux of the total blue light shown in Fig. 6(c), because the absorption coefficient of the blue light is much larger than that of yellow light. The maximum heat generation density q_{max} is located at the center on the incident surface. As a result, the temperature exhibits a similar distribution, namely, T decreases both along z-coordinate and r-coordinate. The maximum temperature T_{max} is located at the same point as the maximum q_{max}. It should be noted that T_{max} is 97.7 degC, which is much lower than the onset quenching temperature (~230 degC for YAG:Ce) [20,29]. In this case, the quantum efficiency will not be affected by the temperature and can be regarded as a constant, which is exactly the assumption in most of the simulations or analytical models for pc-LEDs [17-19]. The above optical performances in the former section are obtained under this case.

As the excitation power keeps increasing, the opto-thermal interaction begins to take effect. Fig. 8 plots the q_{max}, T_{max}, and QE_{min} versus iterative steps under excitation power of (a) 250 mW and (b) 300 mW. In the case of 250 mW, the quantum efficiency corresponding to T_{max} in the first step is slightly lower than the initial one, resulting in a rise of q_{max} and thus a rise of T_{max} in the second step. This rollover lasts seven steps until the temperature keeps unchanged. If we do not consider the opto-thermal interaction, the estimated T_{max} is 213.5 degC. However, the stable T_{max} is 230 degC considering the interaction. This deviation indicates that it's essential to consider the opto-thermal interaction to get more accurate predictions especially under high excitation optical density.

In the case of 300 mW, T_{max} in the first step is beyond the onset quenching temperature, and the QE_{min} shows a rapid drop during the steps, leading to a rapid rise in both q_{max} and T_{max}. This process will not stop because severe thermal quenching occurs, resulting in the failure of the phosphor in the end. In our model, we stop the iterative process once the QE_{min} is lower than 0.5. Fig. 9 shows the three-dimensional distribution of the phosphor temperature and quantum efficiency in the last step. It can be seen that QE(**r**) in the illuminated area is obviously lower than other area and the QE_{min} is only 0.347, indicating a very weak light conversion effect. It should be pointed out that the computational time of the full opto-thermal model is the sum of the computational time of every iterative optical model and thermal model. And it

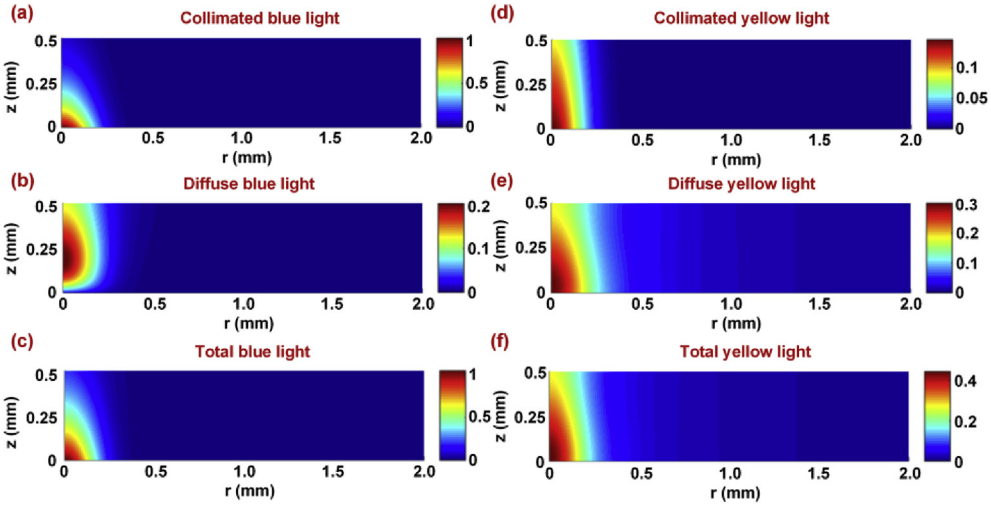

Fig. 6. Two-dimensional radiant flux (W/mm^2) distribution of (a) collimated blue light, (b) diffuse blue light, (c) total blue light, (d) collimated yellow light, (e) diffuse yellow light, and (f) total yellow light.

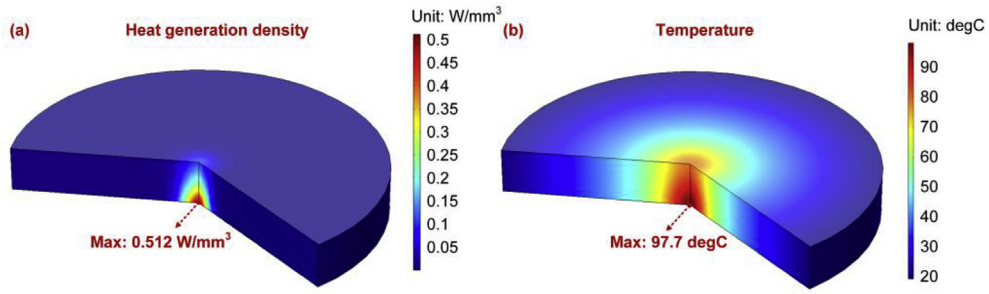

Fig. 7. Three-dimensional distribution of the (a) heat generation density and (b) phosphor temperature under excitation power of 100 mW.

usually takes very short time (about 3 s) to run one thermal simulation. In this case, the whole computational time mainly depends on the iterative steps and the computational time of the optical model. For example, it took about 41 min to run the whole opto-thermal model to obtain the results presented in Fig. 8(b).

4.3. Comparison with experiments

In this section, we compare the experimental results with the model calculations. To make a fair comparison, the boundary conditions in the model need to be consistent with the experimental case. Here, we only point out the different boundaries compared with what has been presented in the above two sections. The excitation power is determined by the measured optical power from LD under varying currents. The cylindrical surface, which is in contact with the metal mount, is set to be a diffuse boundary with a reflectivity of 0.8. The reflectivity is an estimated value of the inner surface of the metal mount. Considering the diameter of the phosphor sample is much larger than the optical path and the spot size, this reflectivity may have little effect on the results. As for the thermal boundary, the phosphor plate together with the mount is simulated to obtain more realistic temperature distribution. The natural convective heat transfer coefficient of 5 W/(m^2·K) is applied on the all the outer surface of the mount and phosphor plate. The thermal contact between the phosphor plate and mount is assumed to be perfect in the simulation. The ambient temperature is measured to be 19.2 degC. The diameter and thickness are the same with the actual values.

Fig. 10 shows the comparisons between the measured and calculated output optical power from phosphor P_{out} and the maximum phosphor temperature on the back surface $T_{max,b}$ under varying driving currents. It should be noted that only the data under current exceeding 150 mA is plotted, which is the threshold current of LD. Above the threshold, P_{out} rises linearly approximately with current due to the increased excitation power. It is observed that there is a non-linearity between the simulated P_{out} between 250 mA and 300 mA, corresponding to the non-linearity of the measured excitation power from LD between 250 mA and 300 mA. In addition, the non-linearity is relatively small, which may be caused by the experimental error. Similarly, $T_{max,b}$ exhibits a constant rise with current due to the increased heat generation density. When the current rises to 450 mA, there is a sudden decrease of P_{out} and a sudden rise of $T_{max,b}$ (374 degC). It should be pointed out that there are a gradual decrease of the measured output optical power and a gradual increase of the measured phosphor temperature with time at 450 mA. We just give approximate values to illustrate the occurrence of the thermal quenching and the absolute values may not make much sense. This is exactly the reason why the error bar of 450 mA is obviously higher than other cases. In addition, the fast degradation and even final carbonization phenomenon of the silicone binder are also observed at 450 mA. The sharp change of P_{out} and $T_{max,b}$ is due to the thermal quenching of YAG:Ce with reduced converted yellow light and silicone degradation with increased absorbed blue and yellow lights.

As for the comparison with experiments, we can see that both the measured P_{out} and $T_{max,b}$ show good agreements with the calculations in terms of similar developing trend. The maximum deviations of measured and calculated P_{out} and $T_{max,b}$ are 11.1% and 12.3%, respectively. This is mainly due to the imperfect estimation of the input parameters, including the absorption and scattering coefficients, quantum efficiency, scattering phase function, and incident irradiance distribution. Also, the smooth surface assumption may not match the real case due to the imperfect fabrication of the phosphor sample. The surface scattering effect can be further considered in our future work by defining the BRDF/BSDF properties of the phosphor surface. In addition, we compare the temperature distribution between them. Fig. 11(a) shows the measured IR image under current of 250 mA. It can be seen that the temperature of the phosphor plate is obviously higher than other areas. We extract and enlarge the temperature distribution of the back surface of the phosphor plate and make a comparison with the calculated one, which are shown in Fig. 11(b) and (c), respectively. Generally speaking, the model and experiment share a similar temperature distribution with a hotspot in the middle and a low-temperature ring in the surrounding area. Fig. 11(d) shows the comparison of the measured and simulated cross-sectional half-circle radial average temperature distribution of the white line plotted in Fig. 11(b) and (c).

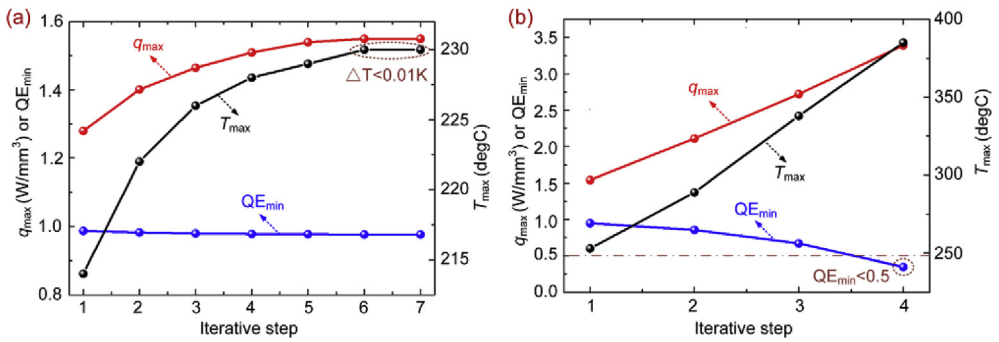

Fig. 8. The maximum heat generation density q_{max}, minimum quantum efficiency QE_{min}, and maximum temperature T_{max} versus iterative steps under excitation power of (a) 250 mW and (b) 300 mW.

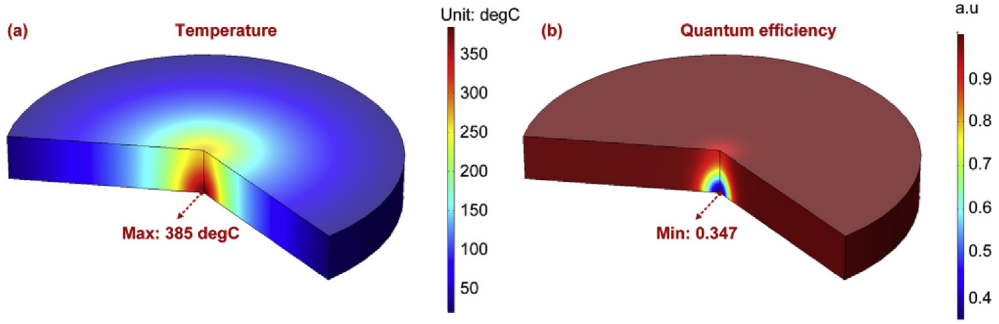

Fig. 9. Three-dimensional distribution of the (a) temperature and (b) quantum efficiency of the phosphor under excitation power of 300 mW, in which case severe thermal quenching occurs.

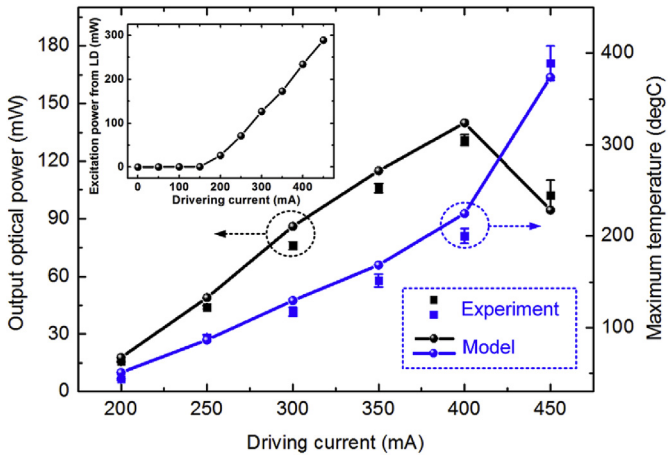

Fig. 10. The comparisons between the measured and calculated output optical power and maximum phosphor temperature on the back surface versus varying driving currents. The inset shows the measured excitation power from LD versus driving currents.

Despite the deviation at the r-coordinate varying from 1 mm to 2mm, which is may be caused by the imperfect estimation of thermal conductivity, they share very close values with each other in general. Therefore, the opto-thermal model is an accurate method to predict the optical and thermal performances of the phosphor.

5. Conclusions

In this work, we present a two-dimensional axisymmetric opto-thermal model for the cylindrical phosphor plate excited by a collimated beam. This model is established by simultaneously solving FRTEs for the excitation blue light and emission yellow light and HDE in the cylindrical coordinate system. The opto-thermal interaction between FRTEs and HDE is achieved by introducing the temperature-dependent phosphor quantum efficiency. A special treatment is made in the collimated incidence by introducing the collimated and diffuse components for the excitation and emission lights. The discontinuous spectral element method is extended to solve FRTEs. By using the model, we obtain the radiance at any spatial location and angular direction and further evaluate the optical and thermal performances. In addition, the opto-thermal interaction plays a significant role under high excitation optical density and needs to be considered to obtain more accurate estimations. Finally, the model is verified by the agreements between the measured and calculated results. In summary, the presented opto-thermal model is an efficient and accurate method to predict the overall optical, thermal and opto-thermal interacted performances of the phosphor and other fluorescent materials.

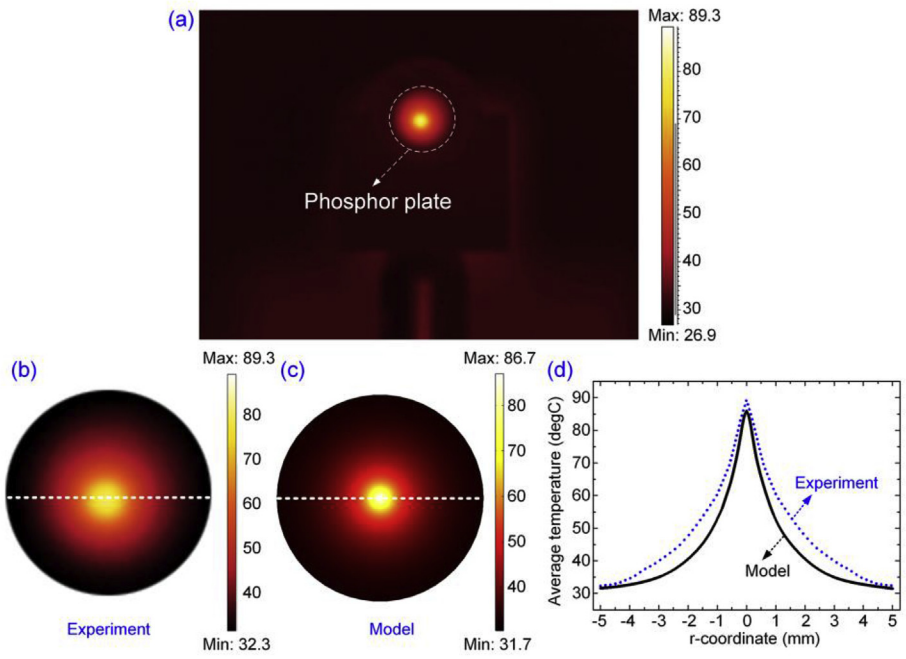

Fig. 11. (a) The measured IR image of the phosphor plate together with the mount; two dimensional temperature distribution of the back surface obtained by the (b) model and (c) IR test, and (d) the comparison between the cross-sectional half-circle radial average temperature distribution. All the results are obtained under driving current of 250 mA. The unit of temperature is degC.

Acknowledgments

The authors would like to acknowledge the financial support by National Natural Science Foundation of China (51625601, 51576078, and 51606074), the Ministry of Science and Technology of the People's Republic of China (Project No. 2017YFE0100600), the financial support from Creative Research Groups Funding of Hubei Province (2018CFA001). Yupu Ma would like to acknowledge Prof. Junming Zhao from Harbin Institute of Technology for providing the original code of DSEM.

Appendix A. Supplementary data

Supplementary data to this article can be found online at https://doi.org/10.1016/j.jlumin.2019.116589.

References

[1] X.B. Luo, R. Hu, S. Liu, K. Wang, Heat and fluid flow in high-power LED packaging and applications, Prog. Energy Combust. Sci. 56 (2016) 1–32.
[2] Y.P. Ma, R. Hu, X.J. Yu, W.C. Shu, X.B. Luo, A modified bidirectional thermal resistance model for junction and phosphor temperature estimation in phosphor-converted light-emitting diodes, Int. J. Heat Mass Transf. 106 (2017) 1–6.
[3] M.A.D. Maur, A. Pecchia, G. Penazzi, W. Rodrigues, A.D. Carlo, Efficiency drop in green InGaN/GaN light emitting diodes: the role of random alloy fluctuations, Phys. Rev. Lett. 116 (2) (2016) 027401.
[4] J.J. Wierer, J.Y. Tsao, D.S. Sizov, Comparison between blue lasers and light-emitting diodes for future solid-state lighting, Laser Photonics Rev. 7 (6) (2013) 963–993.
[5] Y. Peng, Y. Mou, Q.L. Sun, H. Cheng, M.X. Chen, X.B. Luo, Facile fabrication of heat-conducting phosphor-in-glass with dual-sapphire plates for laser-driven white lighting, J. Alloy. Comp. 790 (2019) 744–749.
[6] D.Y. Kang, E. Wu, D.M. Wang, Modeling white light-emitting diodes with phosphor layers, Appl. Phys. Lett. 89 (23) (2006) 231102.
[7] Z.Y. Liu, K. Wang, X.B. Luo, S. Liu, Precise optical modeling of blue light-emitting diodes by Monte Carlo ray-tracing, Optic Express 18 (9) (2010) 9398–9412.
[8] S.W. Jeon, J.H. Noh, K.H. Kim, W.H. Kim, C. Yun, S.B. Song, J.P. Kim, Improvement of phosphor modeling based on the absorption of Stokes shifted light by a phosphor, Optic Express 22 (S5) (2014) A1237–A1242.
[9] A. Correia, P. Hanselaer, Y. Meuret, An efficient optothermal simulation framework for optimization of high-luminance white light sources, IEEE Photonics J 8 (4) (2016) 1–15.
[10] Y.P. Ma, M. Wang, J. Sun, R. Hu, X.B. Luo, Phosphor modeling based on fluorescent radiative transfer equation, Optic Express 26 (13) (2018) 16442–16455.
[11] Y.P. Ma, J. Sun, X.B. Luo, Multi-wavelength phosphor model based on fluorescent radiative transfer equation considering re-absorption effect, J. Lumin. 209 (2019) 109–115.
[12] S. Leyre, G. Durinck, B. Van Giel, W. Saeys, J. Hofkens, G. Deconinck, P. Hanselaer, Extended adding-doubling method for fluorescent applications, Optic Express 20 (16) (2012) 17856–17872.
[13] R. Hu, X.B. Luo, H. Feng, S. Liu, Effect of phosphor settling on the optical performance of phosphor converted LED, J. Lumin. 132 (2012) 1252–1256.
[14] A. Lenef, J. Kelso, Y. Zheng, M. Tchoul, Radiance limits of ceramic phosphors under high excitation fluxes, Proc. SPIE 8841 (2013) 884107–884120.
[15] A. Lenef, J. Kelso, M. Tchoul, O. Mehl, J. Sorg, Y. Zheng, Laser-activated remote phosphor conversion with ceramic phosphors, Proc. SPIE 9190 (2014) 91900C.
[16] X.B. Luo, X. Fu, F. Chen, H. Zheng, Phosphor self-heating in phosphor converted light-emitting diode packaging, Int. J. Heat Mass Transf. 58 (2013) 276–281.
[17] R. Hu, X.B. Luo, H. Zheng, Hotspot location shift in the high-power phosphor-converted white light-emitting diode packages, Jpn. J. Appl. Phys. 51 (9S2) (2012) 09MK05.
[18] B. Yan, N.T. Tran, J.P. You, F.G. Shi, Can junction temperature alone characterize thermal performance of white LED emitters? IEEE Photonics Technol. Lett. 23 (9) (2011) 555–557.
[19] B.J. Shih, S.C. Chiou, Y.H. Hsieh, C.C. Sun, T.H. Yang, Study of temperature distributions in pc-WLEDs with different phosphor packages, Optic Express 23 (26) (2015) 33861–33869.
[20] Y.P. Ma, W. Lan, B. Xie, R. Hu, X.B. Luo, An optical-thermal model for laser-excited remote phosphor with thermal quenching, Int. J. Heat Mass Transf. 116 (2018) 694–702.
[21] A.D. Klose, Radiative transfer of luminescence light in biological tissue, Light Scattering Reviews, vol. 4, Springer, 2009.
[22] L. Zhang, J.M. Zhao, L.H. Liu, Finite element method for modeling radiative transfer in semitransparent graded index cylindrical medium, J. Quant. Spectrosc. RA. 110 (13) (2009) 1085–1096.
[23] J.M. Zhao, L.H. Liu, Discontinuous spectral element method for solving radiative heat transfer in multidimensional semitransparent media, J. Quant. Spectrosc. RA. 107 (1) (2007) 1–16.
[24] L.H. Liu, L. Zhang, H.P. Tan, Finite element method for radiation heat transfer in multi-dimensional graded index medium, J. Quant. Spectrosc. RA. 97 (3) (2006) 436–445.
[25] C.H. Wang, Y. Zhang, H.L. Yi, M. Xie, Analysis of transient radiative transfer induced by an incident short-pulsed laser in a graded-index medium with Fresnel boundaries, Appl. Opt. 56 (7) (2017) 1861–1871.
[26] E.F. Schubert, Light-emitting Diodes, Cambridge Univ. Press, 2003.
[27] X.B. Luo, R. Hu, Calculation of the phosphor heat generation in phosphor-converted light-emitting iodes, Int. J. Heat Mass Transf. 75 (2014) 213–217.
[28] B.F. Shang, Y.P. Ma, R. Hu, C. Yuan, J.Y. Hu, X.B. Luo, Passive thermal management system for downhole electronics in harsh thermal environments, Appl. Therm. Eng. 118 (2017) 593–599.
[29] L.J. Lyu, D.S. Hamilton, Radiative and nonradiative relaxation measurements in Ce^{3+} doped crystals, J. Lumin. 48 (1991) 251–254.
[30] V. Bachmann, C. Ronda, A. Meijerink, Temperature quenching of yellow Ce^{3+} luminescence in YAG:Ce, Chem. Mater. 21 (10) (2009) 2077–2084.
[31] Z.Y. Liu, S. Liu, K. Wang, X.B. Luo, Measurement and numerical studies of optical properties of YAG:Ce phosphor for white light-emitting diode packaging, Appl. Opt. 49 (2) (2010) 247–257.